Radiometric Calibration of Spacecraft using Small Lunar Images

Hugh H. Kieffer, James M. Anderson and Kris J. Becker

U.S. Geological Survey, 2255 N. Gemini Drive, Flagstaff AZ, 86001

ABSTRACT

The Moon is the only object that is accessible to Earth-orbiting imaging systems, whose brightness is within the dynamic range of most such systems, and whose spectral radiance is potentially knowable to a fraction of a percent. As such, it is a desirable target for radiometric calibration. Several spacecraft teams have begun using or are planning to use lunar observations as part of their calibration process. We examine the data reduction steps that can be used to extract the lunar irradiance from low resolution images of the Moon and quantitatively assess the attendant uncertainties. Images of the Moon provide a precise measure of scattered-light sensitivity. The response integrated over an image is compared to a lunar irradiance model being developed from terrestrial multi-band photometric observations over the 350-2500 nm range. For SeaWiFS images, wherein the Moon is about 6 by 20 pixels, the uncertainty in extracting the total lunar signal from the image is about 1% for most bands. A significant source of uncertainty is knowledge of the spacecraft inertial pitch rate, which is currently derived from image analysis. The very low noise in some of the detectors limits knowledge of the zero radiance level to 1/2 of a Data Number. A program is underway to accurately determine at several wavelengths the brightness variations of the Moon associated with Sun-Moon-observer geometry. Comparisons with Earth-based lunar radiometric observations for relative responsivity (changes of spacecraft instrument gain with time) are consistent to about 1/2 the formal uncertainty. At present, the largest errors in using these data for absolute radiometric calibration are in the lunar radiance model.

Keywords: Moon, calibration, spacecraft

1. INTRODUCTION

Imaging the Moon has the advantage of providing a full-aperture calibration of the entire optical and electrical system of an imaging instrument. From Earth's surface, the Moon appears about $\frac{1}{2}^\circ$ in diameter; it is smaller than the field of regard of most orbiting instruments, and discussion here is limited to the case where an instrument acquires an image of the entire Moon. As part of their calibration activities, or inadvertently, a few nominally nadir-pointed spacecraft and many geosynchronous spacecraft have acquired images of the Moon. Low Earth orbit spacecraft have to perform an attitude maneuver, normally done primarily in pitch, to acquire the Moon.

The spectral irradiance from an object such as the Moon can be expressed as:

$$I_\lambda = \int L_{\lambda,x,y} d\Omega \quad , \tag{1}$$

where $L_{\lambda,x,y}$ is the spectral radiance in the instrument spectral range, x and y are orthogonal spatial directions, and Ω is solid angle.

For a normal instrument with discrete spatial sampling and digital radiometric response, the equivalent pragmatic equation for measured irradiance is (dropping the wavelength subscript, this relations holds for each instrument band):

$$I = \sum_m [L_m - \langle L_\mathrm{d} \rangle] \cdot A \quad , \tag{2}$$

where L_m represents the radiance of pixels on the Moon, L_d corresponds to the radiance of the nearby "dark sky" of assumed zero exo-atmospheric radiance, and A is the solid angle represented by a pixel; A must include consideration of the oversampling factor in line and sample directions.

Further author information: (Send correspondence to H.H.K.)
E-mail: hkieffer@usgs.gov; telephone: 520-556-7015; fax: 520-556-7014
J.M.A.: e-mail: anderson@flagmail.wr.usgs.gov K.J.B.: e-mail: kbecker@flagmail.wr.usgs.gov
WWW: http://wwwflag.wr.usgs.gov/USGSFlag/Space/LunarTel/index.html

For simplicity, we will assume that the instrument radiometric response is linear over the range of lunar brightness, and the response can be represented as:

$$N = B + G \cdot L \quad , \tag{3}$$

where N is the Data Number, B is the bias level (zero external input) and G the instrument gain. The effective solid angle for a pixel is:

$$A = \frac{A_c}{f_s} \quad , \tag{4}$$

where A_c is the calibrated (normally ground-based) solid angle represented by one pixel and f_s is the over-sampling factor of the lunar image. Because most spacecraft imaging systems acquire an image by scanning in some fashion, and acquisition of a lunar image commonly involves effective scanning in a manner different than in a normal down-looking scene, f_s may depart significantly from unity. For a multi-band instrument, the oversampling factor is usually identical between bands.

Comparing an instrument response with the lunar irradiance yields the gain:

$$G = \frac{\sum [N_m - < N_d >]}{I_I} \cdot \frac{A_c}{f_s} \quad , \tag{5}$$

where I_I is the lunar irradiance at the instrument.

If more than one detector is involved in a lunar image, their relative gains should be determined and used in processing the lunar image. The processing of the spacecraft image involves, for each band, determining the dark level, deciding which pixels to sum as lunar response, and determining the oversampling factor. A separate task is determining the lunar irradiance at the time and geometry of the image acquisition. A program to develop a lunar irradiance model at a number of wavelengths commonly used in Earth-orbiting imaging systems is underway,[1,2] but is not discussed here.

The accuracy with which one can determine the response of an instrument to the Moon as a source depends upon the angular resolution of the instrument. Lunar calibration views by the Terra spacecraft will involve instruments in which the image of the Moon ranges from sub-pixel (e.g., CERES and MOPITT, these instrument do not intend to use lunar data for calibration) through 6 to 25 pixel diameter (MODIS and MISR) to more than 400 pixel diameter (ASTER-VNIR). Here we discuss processing of existing spacecraft lunar observations with images near 10 pixel extent.

A perhaps obscure but profound reason for the attention to minutiae in this paper is that the current primary source of uncertainty, the lunar radiance model, could decrease by orders of magnitude with time. Because the Moon's reflectance properties are virtually invariant over any time-scale of human interest,[3] future high-accuracy understanding of lunar irradiance could be retroactively applied to current observations, at which time the calibration accuracy will be limited by image analysis methods.

2. AN EXAMPLE OF SMALL LUNAR IMAGES: SeaWiFS

The SeaWiFS instrument has been acquiring lunar images once a month throughout its operations.[4] A lunar image is obtained as the spacecraft executes a pitch turn sweeping past the Moon when the spacecraft is in Earth's shadow and the Moon is approximately 7° from full. The lunar image is normally about 23 lines by 5.5 samples; a typical image is shown in Figure 1. Barnes, Eplee and colleagues have described the calibration of SeaWiFS using the Moon[4–6] and they kindly supplied 100-line by 100-sample extracts of SeaWiFS scenes for the first 13 lunar observations, with the Moon roughly centered in these images. The times and geometries of these observations are shown in Table 1.

Because many images are involved, it is desirable to minimize human interaction in the computer processing, and the processing described here is largely automated. However, a number of decisions need to be made based upon actual in-flight instrument performance, as will be described. Those decisions are represented here by values in parentheses.

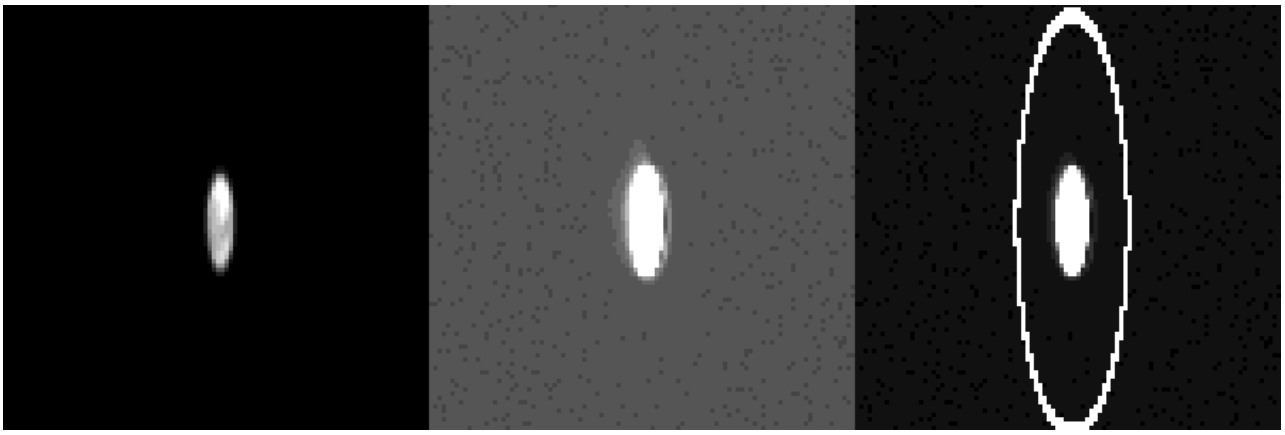

Figure 1. A typical SeaWiFS image of the Moon (File 6, Band 2). A (left): Raw image, unstretched (display range DN 0 to 600). B (center): Strongly stretched to show the extended response; display range is space level -4 to space level +5 DN. C (right): Showing an annulus from bins 48 to 51 (see section 2.1; display range DN 18 to 50).

Table 1. SeaWiFS Lunar Observation Geometry

File	Julian Day		UT		Sun-Moon	S/C-Moon	distance	phase	Libr.
	[-2450000]	Year	Mon	Day	Dist. AU	Dist. km	factor	angle	%
1	767.451	1997	Nov	14	0.9916	361264.	0.8684	-6.78	-0.25
2	797.013	1997	Dec	14	0.9868	371927.	0.9116	-7.09	-0.20
3	826.573	1998	Jan	13	0.9861	383037.	0.9655	-5.49	-0.20
4	855.377	1998	Feb	10	0.9895	390175.	1.0087	6.68	0.05
5	885.074	1998	Mar	12	0.9964	397139.	1.0596	6.76	0.25
6	915.937	1998	Apr	12	1.0051	398678.	1.0867	-6.74	0.45
7	945.565	1998	May	12	1.0128	393846.	1.0767	-7.12	0.55
8	975.055	1998	Jun	10	1.0179	385501.	1.0420	-6.40	0.45
9	1004.544	1998	Jul	10	1.0192	374958.	0.9883	-5.71	0.00
10	1062.496	1998	Sep	5	1.0105	358409.	0.8877	6.68	-0.80
11	1091.918	1998	Oct	5	1.0024	351836.	0.8417	6.83	-1.10
12	1122.028	1998	Nov	4	0.9941	349796.	0.8183	-6.64	-0.80
13	1151.517	1998	Dec	4	0.9880	353870.	0.8273	-7.13	-0.40

2.1. Moon location, size, and shape

The location of the limb of the Moon in the image is needed both to enable the most accurate measures of instrument response to the Moon and to determine the oversampling factor.

The starting point for the non-linear fit used here is estimating the positions of the limbs by locating the center of brightness of the image, and then forming row and column sums along two relatively narrow strips along the cardinal directions of the image centered over this center of brightness. The points where these averages first exceed a given fraction (0.3) of their maximum is chosen as the approximate limb location. The location of the edge of the Moon is further refined by making a first difference image in each cardinal direction, determining the maximum first difference (which usually occurs at the lunar limb), and marking all points where the first difference exceeded a specific fraction (0.3) of this value. Doing this in both directions identifies points that are probably on the limb of the Moon. These points are then fit in a least-squares sense with an ellipse oriented along the image cardinal axes. Points with location residuals more than (7) standard deviations from the best-fit limb are eliminated on each iteration, until the number of points stabilizes or the total error stops decreasing. The center and the semi-major axis of the final ellipse are maintained as floating-point numbers to sub-pixel accuracy.

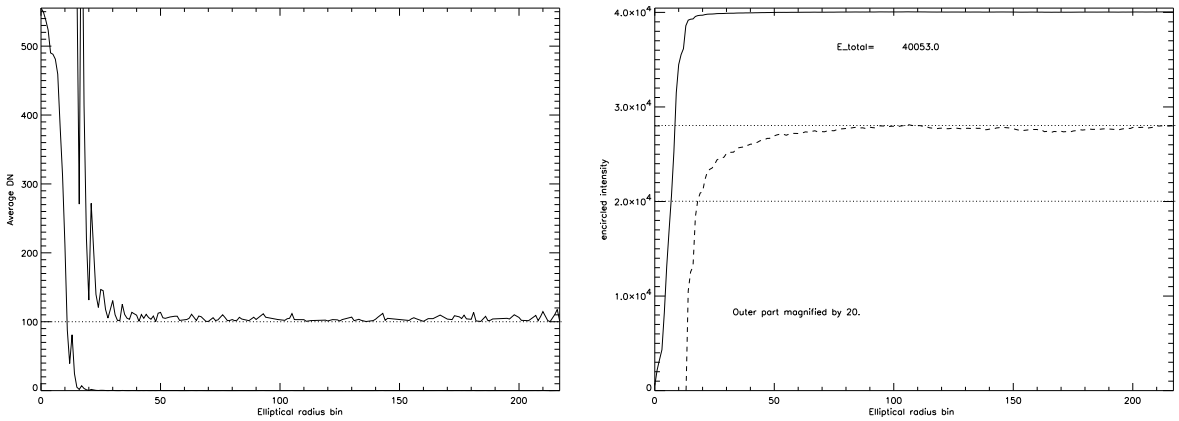

Figure 2. Summation results for elliptical annuli centered on the Moon; File 2, Band 2. The bin radius units are $q = 2$ per image pixel, as described in the text. The Moon's radius is about 10 bins. A (left). Average DN minus space DN for each annulus; the upper line is a 100-fold magnification, with offset zero level. B (right). Encircled intensity. For a uniformly bright disk, the curve would rise quadratically to a sharp limit. The dashed curve is a 20-fold enlargement of the curve; the dotted lines are separated by 1%. The behavior is an excellent measure of light scattering in the instrument.

Each pixel is then assigned an annulus index as the nearest integer to:

$$r = c\sqrt{\left(\frac{x - x_0}{R_x}\right)^2 + \left(\frac{y - y_0}{R_y}\right)^2} \quad , \tag{6}$$

where x_0, y_0 is the center position, R_x and R_y are the semi-major axes, and $c = q\sqrt{R_x R_y}$ is the number of bins from center to limb; q is an arbitrary spatial resolution factor, it was set to 2. Because the phase angles are 7° or less, the illuminated Moon is out-of-round by only 0.5%. At larger phase angles, the first-difference test will blank out the terminator.

In addition to the small ghost image present in each band, all bands have a small dip in intensity about four pixels to the right (increasing sample) of the center of the Moon. The next sample is typically about 5 DN greater than the value in this local minimum.

2.2. Dark Level

Accuracy in determining the dark level of an image can be important because measuring the total response to an object may involve summing a significantly larger number of pixels than just the geometric extent of the object. Of the many possible approaches, we chose to average an elliptical annulus centered around the Moon but well outside the lunar image. This minimizes the influence of background drift. A corrected average was found by including only data within (4) standard deviations of the mean, thus excluding any noise spikes. A conservative location for this annulus was determined by examining the average value in a series of narrow elliptical annuli from the center to the edge of the image. The lunar limb is approximately at annulus bin number 10 (see Figure 2). An ellipse in these images represents a circle in terms of scattered light sensitivity for the instrument. Figure 2B shows that a weak zone of scattered light extends out to several lunar radii; the encircled intensity curve reaches to within 1% of its maximum by 2 radii from the Moon's center and 0.1% at about 5 lunar radii (1° from the edge of the Moon). For this work, the annulus range for the dark level was chosen as from 100 to 150. The largest annulus that fits entirely within the 100 by 100 sub-image available here has a bin index of about 52. To use an annulus that captured scattered light to the 0.1% level would require files of about 200 lines.

The difference between this measure of the dark level and simple averages of the image borders was less than 0.02 DN for nearly all images. There is no detectable dependence of dark level on line number.

For most bands, there is a rise of about 8 DN for one sample, on the high sample side, beyond the lunar limb. This is related to a known instrument characteristic[7] (E. Eplee, personal communication).

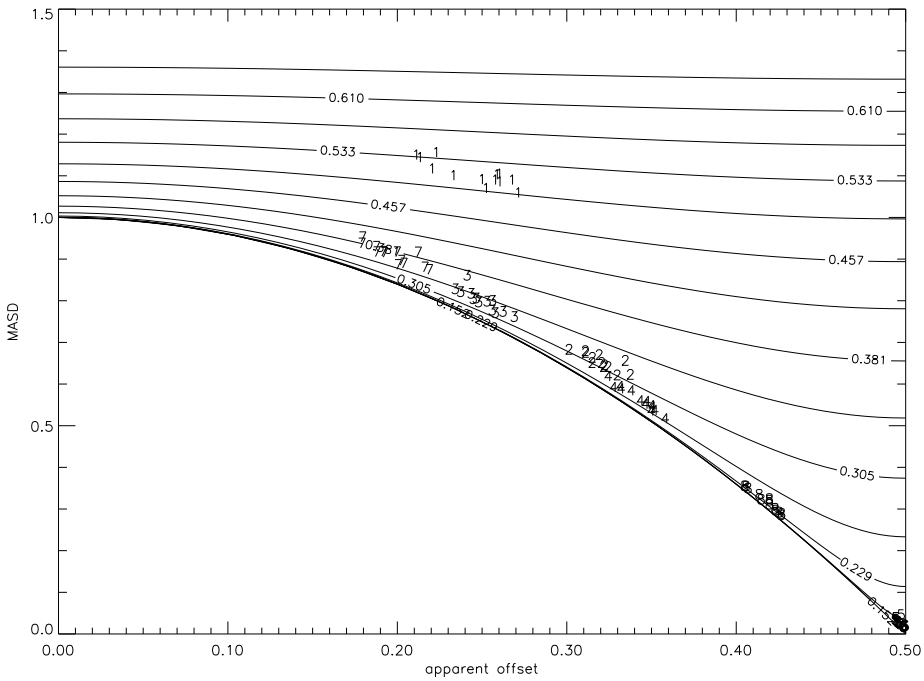

Figure 3. The relation between parameters measurable in a digital system and the true noise level. The abscissa is the observed average, as an offset from the nearest $\frac{1}{2}$ integer value, and the ordinate is the measured mean absolute second difference (MASD). The curves are contours for evenly spaced values of standard deviation from 0.15 to $\sqrt{2}$, above which the analog relation between MASD and σ is closely approximated. The single-digit numbers show the values for the 8 SeaWiFS bands measured during SeaWiFS views of the Moon; bands 5 and 6 are indiscernibly clustered at the lower-right corner.

2.3. Noise level

The detector noise level was determined using the first and last (25) samples of each line, an area which excluded any signal from the Moon. The noise level was determined first as the standard deviation of the data in this border region, and then as the standard deviation of these data excluding outliers defined as being more than (5) standard deviations from the mean.

2.4. Limitations of low-noise systems

The quantitative determination of noise and of dark level for detectors with standard deviations less than 0.5 DN can be strongly influenced by the fact that these are digital measures of an analog signal. In essence, as the noise diminishes toward zero, the uncertainty in the dark level approaches 0.5 DN. The digitization process has been modeled for normally distributed data, and the theoretical relation between the observed noise and bias level, and the true noise and bias levels, has been determined. The critical parameter is the offset of the true bias level from the nearest analog-to-digital converter (ADC) switching level. Figure 3 shows the relation between apparent bias level and the true bias level as a function of detector noise level.

Throughout this work, we have determined the apparent detector noise level as the mean absolute second difference (MASD) of dark data. Using the MASD to determine noise avoids any dependence upon slow drift (none is apparent in SeaWiFS data); for normally distributed data, the MASD is $\sqrt{12/\pi} = 1.9544$ times the standard deviation. At low noise levels, MASD < 1 or standard deviation (σ) < 0.5, the apparent mean can deviate by up to $\frac{1}{2}$ DN from the true mean. Also, the mean absolute second difference can become a strong function of the mean offset (from the nearest switching level; see Figure 4). Modeling of the MASD and the apparent offset was done by calculating the probability of all possible 3-long sequences using the Gaussian distribution function.

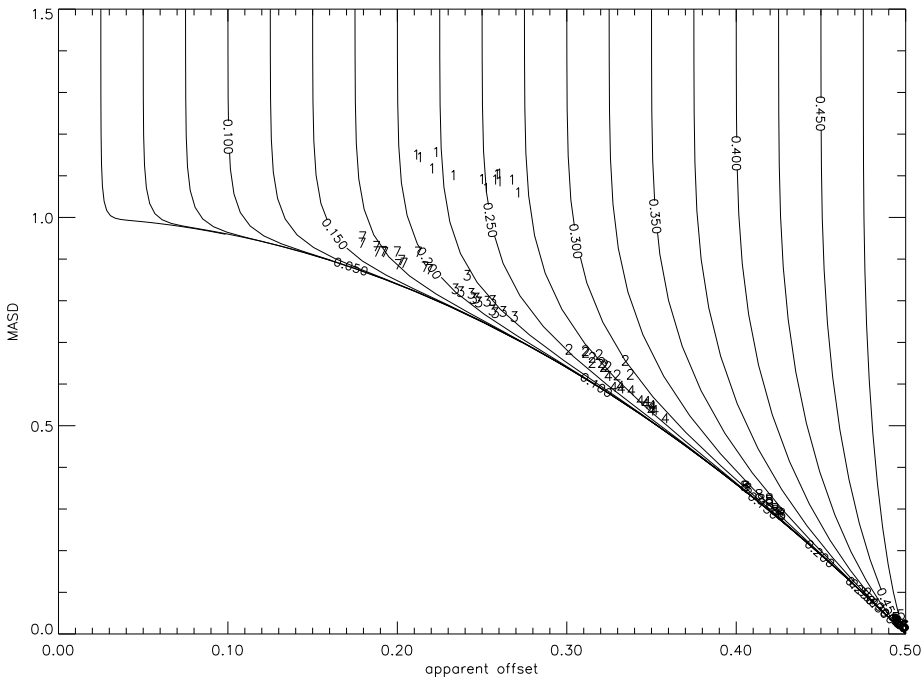

Figure 4. The relation between parameters measurable in a digital system and the true bias level. The axes are as in Figure 3. The curves are contours of true offset uniformly spaced from 0.025 to 0.475. The single-digit numbers show the values for the 8 SeaWiFS bands measured during 13 views of the Moon. As the detectors approach the theoretical line for zero true noise, the offset level becomes less well-determined and is highly uncertain for band 8. Bands 5 and 6 are indiscernably clustered at the lower-right corner.

The uncertainty in the true dark level d^* is:

$$U_{d^*} = U_d \left(\frac{\partial d^*}{\partial d_0} \right)_{d_o,\beta} + U_\beta \left(\frac{\partial d^*}{\partial \beta} \right)_{d_o,\beta} \quad , \tag{7}$$

where d is the measured dark level, d_0 is the offset of the measured dark level from the nearest $\frac{1}{2}$ integer level, and β is the measured MASD. $\frac{\partial d^*}{\partial d_o}$ is 1 for large σ, and approaches 4 for low σ; $\frac{\partial d^*}{\partial \beta}$ is zero for large σ and approaches ∞ for small σ.

Bands 5 and 6 have MASD levels so low that it is effectively impossible to determine the true noise level or the true offset. Band 8 has a true noise level of about 0.22 DN; the offsets are probably less than 0.3, but cannot be determined accurately.

2.5. SeaWiFS bands

The consistency of true offset for those bands where it can be determined with some reliability, eg, bands 1 and 7, suggest that this behavior also holds for the other bands. For band 8, the offset from the ADC switching level could be any value up to approximately 0.3 DN. For bands 5 and 6 the offset is unconstrained: ie, it could be any value from 0 to 0.5, and the sign of the true offset is uncertain. Thus, for bands 5 and 6, the dark level is uncertain by $\pm\frac{1}{2}$ DN.

The annular sums provide an excellent measure of scattered light sensitivity. The individual profiles are generally consistent for each band at the level of $\sim 0.05\%$. Figure 5 shows the average normalized response profile for each band, averaged over all files. The semi-minor axis used was the average over all images, and for each file $\frac{1}{2}$ the average chord length was used for the semi-major axis. For Bands 5,6,8 and 2, the apparent sharpness of the scattered-light rejection may be partially due to the low noise level of these bands, wherein less than 1 full DN increase above the space level may not increase the digital output. The results could be slightly improved by having more lines in the images.

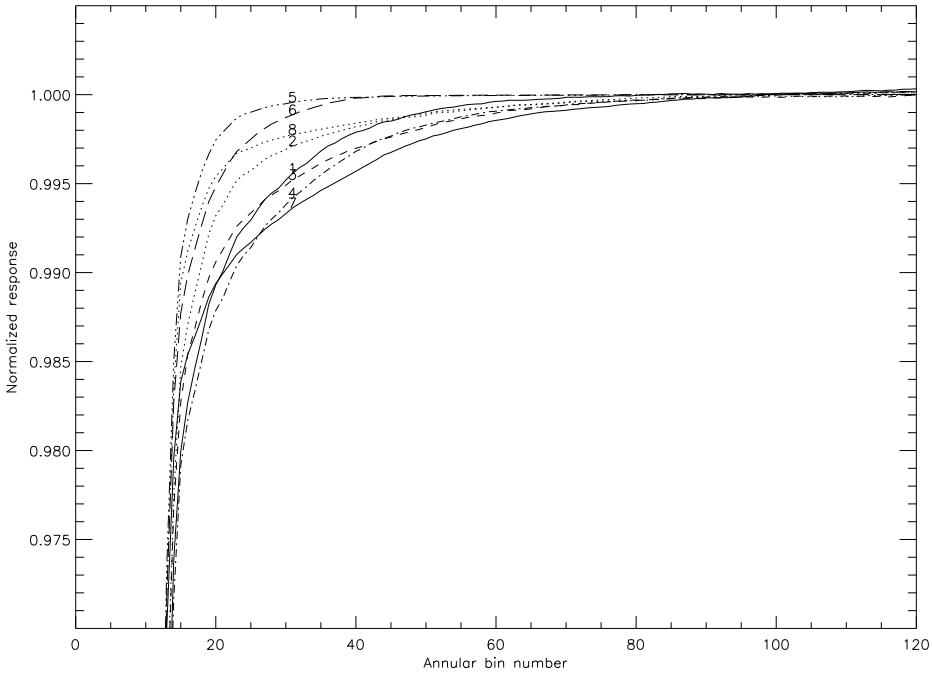

Figure 5. The scattered-light sensitivity of SeaWiFS bands based upon lunar observations. Results for each band were averaged over 13 observations. The abcissa scale is 1 bin $= \frac{1}{2\sqrt{\text{elongation}}}$ pixel in the sample direction ≈ 0.42 mrad. Bands 5,6,8 and 2 may appear better than actual, see section 2.5.

2.6. Intensity sums

The "intensity," or the sum of the apparent signal from the Moon, $T \equiv \sum [N_{\rm m} - < N_{\rm d} >]$, can be determined in several ways. The most straightforward way is simply to sum all pixel values minus the average space value; this method does not require a detailed location of the Moon but is the most sensitive to errors in the space level and will include the noisiest points. A better estimate is a similar sum of all pixel levels above an average space value for a rectangular box centered on the Moon and extending beyond the nominal limb by a given number of pixels (e.g., 15). This should be made large enough to include the "ghost" image of the Moon due to scattering in the instrument. This ghost is displaced toward higher sample numbers for the odd-number detectors and toward lower sample numbers for the even-number detectors.

A more precise estimate of intensity can be made by forming the cumulative sum of energy above the space level in increasing large elliptical annuli centered on the Moon. The average value in these annuli drops dramatically near the edge of the Moon, and hence the cumulative sum rapidly approaches its maximum. For this measure of flux, the dark level can be chosen as the average of a zone of annuli well beyond the limb of the Moon. Figure 2A shows a typical plot of the average and Figure 2B the cumulative sum as a function of elliptical distance from the center of the Moon. For this work, the average of bins 100 to 150 were used for the space level, and the intensity was summed out to bin 60. The intensities for all Files and Bands are listed in Table 2.

2.7. Consistency of intensity

Because of the low noise and stable dark level, the measures of intensity using a rectangular box or the elliptical annuli typically differ by less than one part in 10 000. There are 2 700 pixels in the annular intensity sums used here, and the DN sums are typically on order of 50 000 DN, so that an uncertainty in the space level of 0.5 DN would contribute an uncertainty in intensity of 2.5%. Using an annulus bin limit of 45 would involve 1 630 pixels, decreasing the sensitivity to uncertain dark level by a factor of ≈ 1.6.

Normalizing each file to the average of bands one through six, it seems that the responsivity of these six bands has varied less than 0.3% amongst the 13 images, the responsivity of band seven has dropped by 1.4% and the responsivity of band eight has dropped by 4.9%. Most of these changes occurred prior to file 9.

Table 2. Intensity of Lunar Images (units of 100 DN)

File	Band 1	Band 2	Band 3	Band 4	Band 5	Band 6	Band 7	Band 8	mean	std.dev
1	488.27	482.29	484.77	495.24	517.52	502.83	537.18	501.05	501.14	18.49
2	467.55	460.67	463.16	473.06	495.25	481.52	513.49	477.98	479.08	17.79
3	473.50	467.21	468.65	478.34	499.50	483.73	514.45	476.24	482.70	16.36
4	431.95	427.28	429.18	439.09	458.61	445.33	473.76	437.49	442.84	16.04
5	409.62	404.94	406.90	416.00	433.87	421.19	447.21	411.04	418.85	14.76
6	404.96	400.53	402.74	411.06	429.37	415.55	440.92	402.83	413.50	14.56
7	420.86	416.20	418.32	428.41	447.04	432.50	458.72	417.44	429.94	15.55
8	451.31	446.15	447.54	457.48	477.70	461.89	488.56	443.56	459.27	16.16
9	488.02	482.35	483.63	494.83	515.79	497.96	524.87	475.33	495.35	17.14
10	521.33	516.23	518.53	530.73	553.22	536.00	564.69	509.39	531.27	19.22
11	548.73	543.19	545.15	558.55	582.37	564.61	594.23	536.22	559.13	20.30
12	557.47	551.75	554.61	566.89	592.28	573.52	604.53	544.34	568.17	20.94
13	531.05	524.89	528.54	540.40	564.94	547.00	577.48	519.30	541.70	20.43
mean	476.51	471.05	473.21	483.85	505.19	489.51	518.47	473.25	486.38	17.52

3. EPHEMERIS

The geometric data contained in the files is shown in Table 1, along with the Julian Date of the time for each file. The SeaWiFS observations are at monthly intervals except for a 2 month gap between Files 9 and 10. The astronomical ephemeris computer program MICA[8] was run for each of these Julian dates, producing the geocentric equatorial position of the Moon and the Sun in the mean equator and equinox of J2000, along with the rotation and illumination parameters for the Moon in the true equator and equinox of date. From these, the detailed observation geometry for SeaWiFS is calculated. The phase angle at the center of the Moon was calculated from the dot product of the Sun-Moon and the SeaWiFS-Moon vectors. The direction of the lunar north polar spin axis and primary meridian is based upon IAU formulae.[9] The sub-spacecraft selenographic coordinates were computed from the Moon-SeaWiFS vector and Moon orientation in J2000. The lengths of the Sun-Moon vector and the SeaWiFS-Moon vector were used to calculate the distance normalization factor. The motion of the spacecraft during acquisition of an image is ignored; SeaWiFS acquires a lunar image in less than 4 sec.

3.1. Over-sample factor

For a constant angular rotation velocity of the spacecraft, the apparent response of an instrument to the Moon depends linearly on the length of time spent crossing it. Absent accurate information on the spacecraft pitch rate during a lunar maneuver, this must be derived from the images themselves.

In addition to the ellipse-fit described above, the size of the Moon in the line direction was determined as the separation of the locations of the extreme top and bottom limbs. These were each determined by fitting a quadratic function to the three outermost edge locations determined as the locations, using linear interpolation, of topmost and lowest points where the brightness in that column was ($\frac{1}{2}$) the value 3.0 pixels closer to the center of the Moon (Table 3). These sizes average 20.5 pixels, 1.0% smaller than major axis of the ellipse fits. The standard deviation between bands averaged 0.08 out of 20.5; considerably more consistent than $\sigma = 0.21$ for the average semi-major axis of 10.35 for the ellipse fits.

The apparent size of the Moon in the line direction was quite consistent between bands, indicating little light scattering in that direction. We have used the average across bands. Various band-averaged values are shown in Table 3. The first pair of columns are the semi-major axis and its fractional uncertainty (the standard deviation divided by the mean). The next pair are similar results for the extent of the image in the line direction derived as described above. The next column is the ratio of the line-extent to the ellipse semi-major axis. The "elongation" column is the ratio of semi-major to semi-minor axes based upon ellipse fitting; next column is the standard deviation of this value across bands.

The size of the Moon in the sample direction is not well estimated because of its small extent, 2.8 pixels; the average value of the fractional uncertainty was 4%.

Table 3. Size and Shape of Moon in Images

File	semi-major	fract. uncert.	# lines diam.	fract. uncert.	diam/ major	elong-ation	std. dev.
1	10.009	0.006	20.179	0.002	2.016	3.414	0.100
2	10.152	0.016	19.800	0.004	1.950	3.780	0.124
3	9.687	0.018	19.398	0.008	2.002	3.532	0.116
4	9.686	0.006	19.075	0.007	1.969	3.868	0.063
5	9.599	0.033	18.623	0.005	1.940	3.300	0.110
6	9.525	0.023	18.777	0.006	1.971	4.175	0.297
7	10.426	0.034	19.920	0.003	1.911	3.663	0.253
8	10.624	0.017	20.576	0.003	1.937	3.676	0.108
9	10.737	0.043	21.102	0.002	1.965	3.897	0.534
10	10.930	0.028	22.149	0.002	2.026	3.769	0.177
11	10.807	0.016	22.628	0.002	2.094	3.795	0.089
12	11.268	0.018	22.488	0.005	1.996	3.672	0.207
13	11.121	0.010	21.777	0.003	1.958	3.653	0.068
mean	10.351	0.021	20.499	0.004	1.980	3.707	0.173
sdev	0.612		1.410		0.048	0.221	

Using the ephemeris-based angular size of the Moon yields a mean pixel size in the sample direction of 1.66 mrad, surprisingly close to the published value of 1.6 mrad.[4] The extent of the Moon in the line direction was taken as the average of the ellipse fit and the central chord length, which yields a mean over-sample factor of 3.70. The images suggest that the spacecraft pitch rate had a standard deviation of 3.7%.

4. CALIBRATION WITH LUNAR IRRADIANCE

The lunar irradiance at unit distance, $I_{\oslash}$, is estimated from the polynomial fit to the ground-based measurements[2]:

$$\ln I_{\oslash} = \sum_{i=0}^{3} (c_i + d_i\lambda) g^i) \quad , \tag{8}$$

where λ is the band wavelength and g is the viewer-Sun phase angle for each file. The coefficients c and d can be different for the waxing and waning Moon. Lunar libration has not yet been incorporated in reduction of the RObotic Lunar Observatory (ROLO)[1] observations; its value (δ) has been modeled to be on the order of 2%, and comparable to the current residuals of the ROLO reduction.[2] Initial analysis indicates that it is not a strong function of wavelength for the phase angles used by SeaWiFS. The values shown in Table 1 were derived using the model shown in Kieffer and Anderson, 1998.[2]

The over-sample factor is:

$$f_{\rm s} = \frac{Y}{Y_{\rm nom}} \cdot \frac{D_{\rm I}}{D_{\oslash}} \quad , \tag{9}$$

where Y is the extent of the Moon in the image in the line direction, $Y_{\rm nom}$ is the expected image size of the Moon for no over-sampling at nominal distance $D_{\oslash}$, and $D_{\rm I}$ is the instrument-Moon distance. The nominal conditions are $D_{\oslash}$ = 384400 km, the mean radius of the Moon's orbit, and $Y_{\rm nom}$ = 5.65, the number of pixels expected for the Moons diameter at $D_{\oslash}$ distance for a 1.6 mrad pixel.

The scaling to standard distances is:

$$f_d = \left(\frac{D_{\rm I}}{D_{\oslash}}\right)^2 D_{\odot}^2 \quad , \tag{10}$$

where $D_{\odot}$ is the Sun-Moon distance in Astronomical Units.

The instrument responsivity is then:

$$G = \frac{T \cdot A_{\rm c}/f_{\rm s}}{I_{\oslash}(1+\delta)} f_d \quad , \tag{11}$$

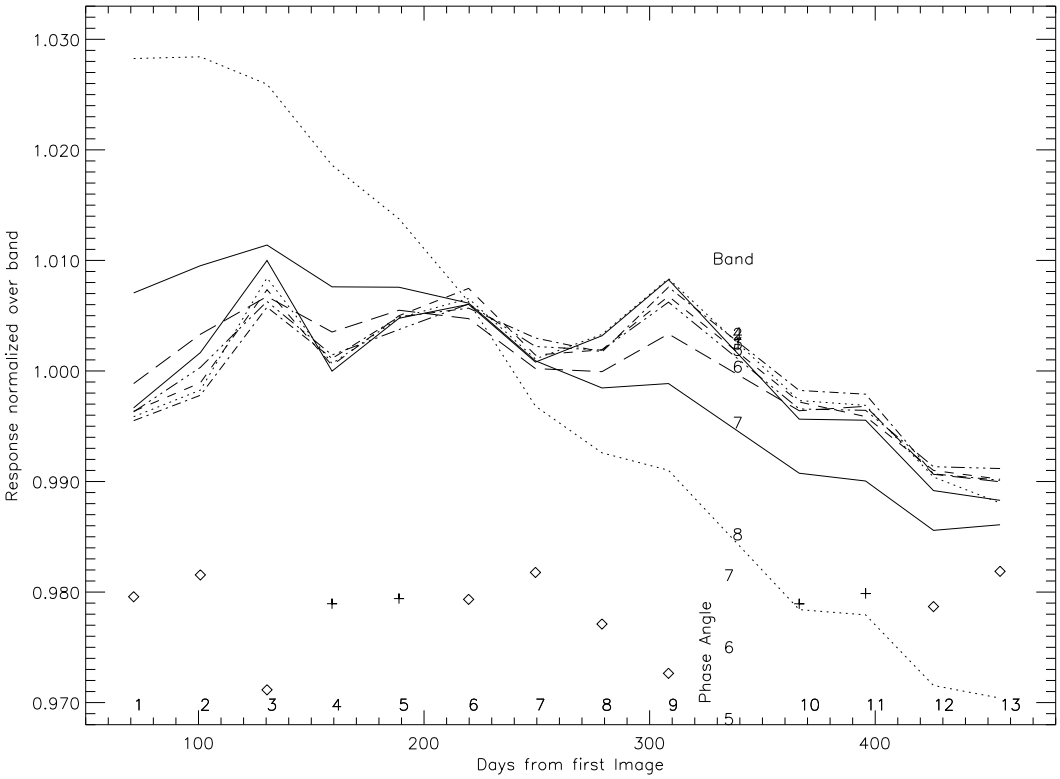

Figure 6. The relative responsivity of SeaWiFS bands from lunar images. Each band has been normalized over all files. The phase angle is represented by symbols near the bottom of the figure, with diamonds before full Moon and crosses after full Moon; the values are listed in Table 1.

where T is the intensity of the SeaWiFS lunar image and δ is the libration correction.

Figure 6 shows the resulting comparisons to SeaWiFS. The change in lunar irradiance with phase was then estimated using a preliminary model derived from ROLO observations with phase angles from 4° to 30° (Figure 7). The dominant remaining variations are not related to lunar brightness variations, but must be associated with poor measures of the over-sample factor. A similar pattern of correlated changes between bands is seen in the analysis of Barnes et al.[4] The results here show more scatter than those derived by Barnes and colleagues[4–6]; the reason for this difference remains obscure.

If the response values for each file are normalized to the average of Bands 1 through 6, these bands are seen to be consistent to within 0.5% (Figure 8). Band 7 had a response drop of about 1.8% over the first 300 days then recovered slightly, and Band 8 response has dropped 5% over the observation period, relative to the first 6 bands. The consistency of the response of the first 6 bands indicates that lunar observations have the potential to produce calibrations to the level of a few tenths of a percent.

5. ERROR ANALYSIS

Referring to Equations 5 and 11, the fractional uncertainty in instrument gain G, U_G, determined by observation of a finite source is composed of several parts:

- The fractional uncertainty of the solid angle factor A, U_A. For lunar views, this is virtually the uncertainty in the elongation of the image.
- The uncertainty in the intensity sum, U_T, which itself is composed of two parts, the probable error of the sum of Data Numbers for pixels sensing the Moon, E_S, and the probable error of the average dark level, E_d.

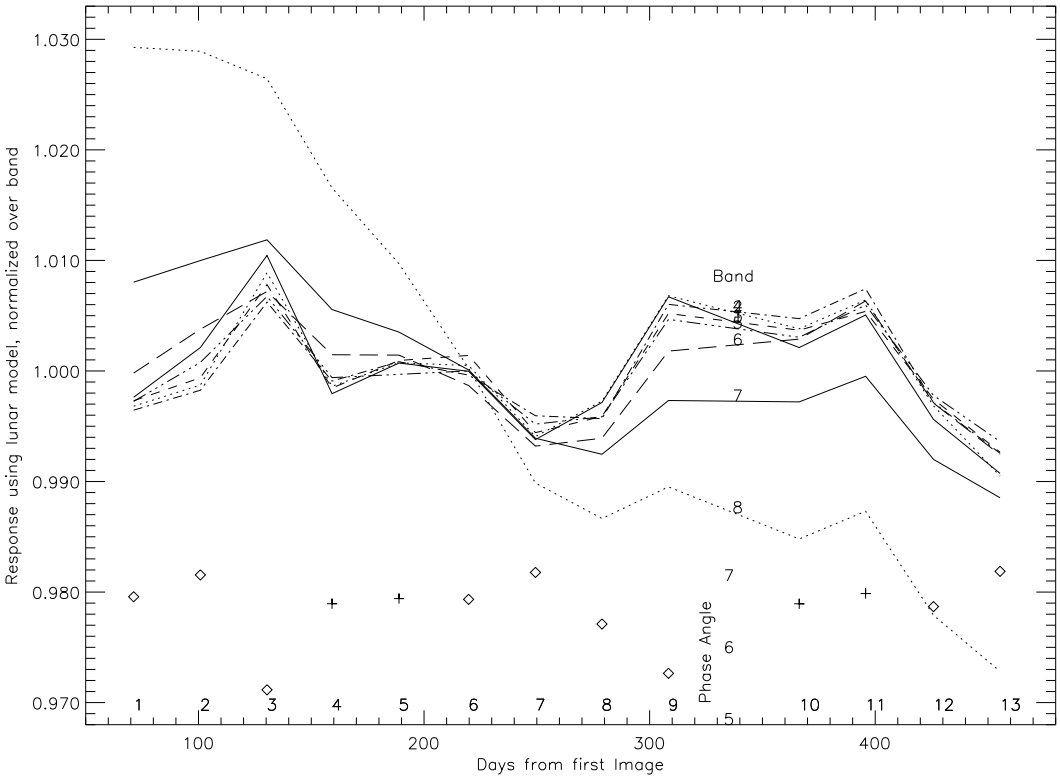

Figure 7. The responsivity of SeaWiFS bands based upon lunar observations using the preliminary ROLO lunar model over small phase angles. Each band has been normalized over all files. The phase angle is represented as in Figure 6. Band 8 shows a net downward trend of almost 6%.

- The uncertainty in the irradiance level of the source, U_I. For lunar calibration, this is composed of two parts. The geometric portion is twice the sum of the normalized uncertainties of the Sun-Moon and the spacecraft-Moon distances; as these distances are expected to be known to better than 2 ppm, this uncertainty is negligible. The fractional uncertainty of the lunar radiance at standard distance is the dominant term, and has both static and temporal components. Observing at similar phase angles minimizes the influence of the temporal component.

The probable error in the average $\langle N_\mathrm{d} \rangle$ of M_d dark pixels is $E_d = \Delta + \sqrt{(\sigma^2 + 1/12)/M_\mathrm{d}}$, where Δ is the correlated dark error (the difference between the apparent and true dark levels associated with low-noise detectors), and σ is the true detector noise level. We will ignore read noise and photon-statistics noise for SeaWiFS. The $1/12$ term is digitization noise. Because the Moon is variegated in brightness, the errors contributing to the sum $\sum N_\mathrm{m}$ of M_m Moon pixels can be treated as uncorrelated, $E_S \sim \sqrt{M_\mathrm{m}}\sqrt{\sigma^2 + 1/12}$. Then, the fractional error in T is

$$U_T \sim \frac{E_S + M_\mathrm{m} E_d}{T} + O_T \quad , \tag{12}$$

where O_T is the fraction of the lunar signal omitted because it lies outside the summation area. Thus, the fractional error in T is a minimum at some compromise between keeping the lunar summation region small to reduce correlated dark level errors and expanding it to include the wings of the point spread function. Ideally, there would be no scattered light, and the sum would need to extend only over the geometric Moon.

Presuming that these parts are uncorrelated, then:

$$U_G^2 \approx U_A^2 + U_T^2 + U_I^2 \quad . \tag{13}$$

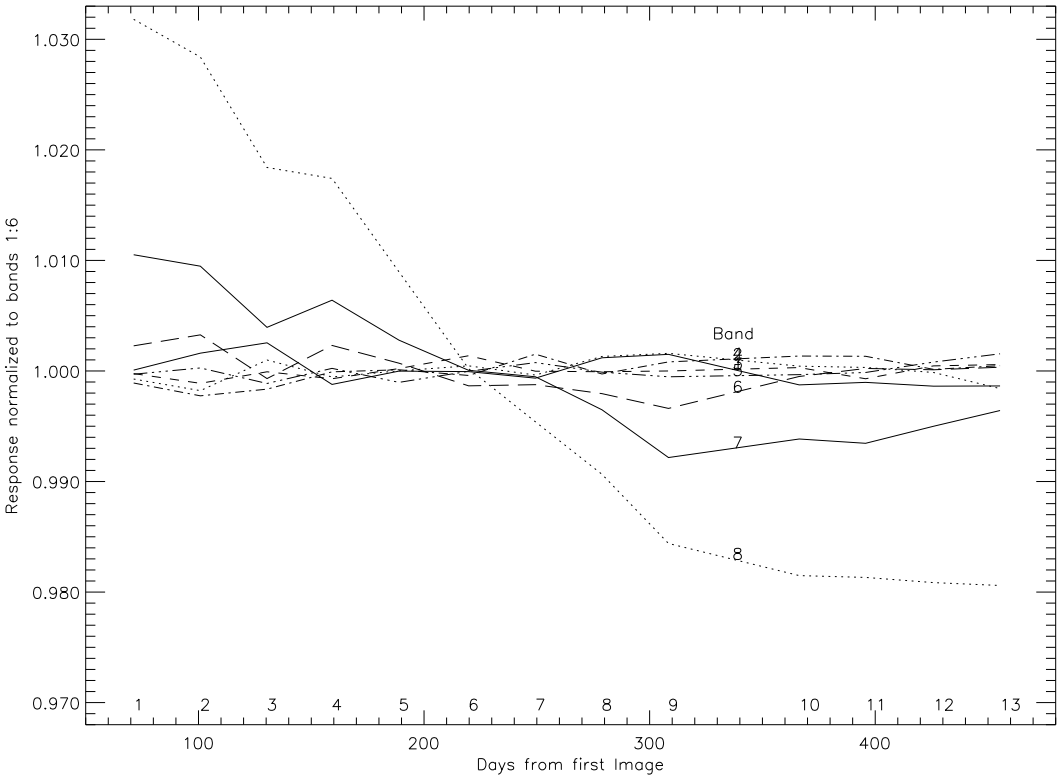

Figure 8. The responsivity of SeaWiFS bands based upon lunar observations, normalized over the average response of Bands 1 to 6.

5.1. Estimated errors

The standard deviation over the 8 bands of the over-sampling factor determined by chord length averages 0.5% over the files processed here. This is probably a reasonable assignment of error to the over-sample factor.

For U_T, the size of the summation areas is important. The number of samples on the Moon (inside the fit ellipse) averages 91. For all bands, $M_{\rm m} = 2\,695$ and $M_{\rm d} = 2\,728$. We will look at two limiting cases. The average DN difference between Moon and space is 534. Referring to Figure 4, in Band 1 $\sigma \approx 0.5$ and $\Delta = 0$; E_S and $M_{\rm m}E_d$ are both about 30. For Band 5, $\sigma < 0.2$ and $\Delta = 0.5$; $E_S = 18$ and $M_{\rm m}E_d = 1365$. Refering to Figure 5, the fraction of irradiance outside of the summation area is about 0.02%. With $T \sim 50\,000$ in Band 1 and $\sim 42\,000$ in Band 5, $U_T \approx 0.3\%$ and $\approx 3.5\%$, respectively. In the "low-noise" case, uncertainty is actually much higher.

The uncertainty in the preliminary lunar radiometric model is on the order of 5%, but the uncertainty in the slope of the phase curve over the small range of angles used by SeaWiFS is certainly much smaller, and we conservatively assign an uncertainty of 1%. The difference between waxing and waning quarters for 7° phase is not independently known at the level of accuracy of interest here. To the extent that the shape of the lunar surface photometric function does not vary between the mare (dark) and highland (bright) areas, there would be no effect except due to changing proportion of mare in the observed hemisphere. But this is the libration effect, which has been included.

With these values, Equation 13 for [Band 1 | Band 5] becomes:

$$U_G^2 \approx 0.005^2 + [\ 0.003 \mid 0.035\ ]^2 + 0.01^2 \qquad \text{or} \qquad U_G = [\ 1.2 \mid 3.7\ ]\% \ .$$

The lower estimate is similiar to the variation seen in Figure 7. Bands 5 and 6 vary between files much less than indicated by the second estimate. This must indicate that the bias level for those detectors is very stable, and the response uncertainty associated with the true offset level remains hidden. Currently, the first and third terms of Equation 13 dominate. It is important to reduce the uncertainty in the over-sampling factor; this may be possible by examination of the spacecraft engineering data recorded during the lunar maneuvers. For the instruments on the

Terra spacecraft, it can be determined about a factor of 100 better using the high-resolution images from ASTER, wherein the Moon will extend about 2000 lines. We anticipate that the uncertainty in the absolute lunar irradiance model will reach 2% within the next 2 years. If SeaWiFS observations were confined to nearly the same time relative to full Moon each month, only the libration terms would be important, and that will be known to much less than 1%.

6. CONCLUSIONS

The response of a spacecraft imaging system to the Moon can be accurately determined even if the lunar image is as small as 90 pixels in area. Accuracy could be improved beyond the analysis here by judicious choice of the summation area; compromising summing the weak outer wings of response for minimizing the number of pixels summed. However, absolute calibration can be limited by the accuracy information of the turn rate of the spacecraft, which is difficult to extract accurately from such small images. Instruments planning lunar calibration views should acquire the engineering data on inertial turn rates if those may be known to the percent level. If the uncertainty in turn rates can be reduced, as the absolute lunar radiance model improves, the calibration accuracy of systems with low noise levels ($< \frac{1}{2}$ DN) may be limited by uncertainty of the dark level.

Uncertainty of the lunar irradiance can be minimized by using a small range of phase angles, preferably on the same side of Full Moon. The observation history with SeaWiFS suggests that determination of relative stability between bands can be done to 0.1% using the Moon as a source. For very low-noise detectors, uncertainty of the true dark level remains a hidden source of error.

ACKNOWLEDGMENTS

The SeaWiFS images data were provided by Gene Eplee. T.N. Titus contributed to development of the behavior of low-noise detectors. Discussions with R. Barnes have been helpful and ever pleasant.

REFERENCES

1. H. H. Kieffer and R. L. Wildey, "Establishing the moon as a spectral radiance standard," *J. of Atmospheric and Oceanic Technology* **13**(2), pp. 360–375, 1996.
2. H. H. Kieffer and J. A. Anderson, "Use of the moon for spacecraft calibration over 350–2500 nm," *Proc. SPIE* **3438**, pp. 325–335, 1998.
3. H. H. Kieffer, "Photometric stability of the lunar surface," *Icarus* **130**, pp. 323–327, 1997.
4. R. A. Barnes, J. R. E. Eplee, F. S. Patt, and C. R. McClain, "Changes in the radiometric response of SeaWiFS determined from lunar and solar-based measurements," *Ap. Opt* **38**, pp. 4649–4664, 1999.
5. R. A. Barnes, J. R. E. Eplee, and F. S. Patt, "SeaWiFS measurements of the moon," *Proc. SPIE* **3438**, pp. 311–324, 1998.
6. R. A. Barnes and C. R. McClain, "The calibration of SeaWiFS after two years on-orbit," 1999. these proceedings.
7. R. A. Barnes, A. Holmes, and W. Esaias, "Stray light in the SeaWiFS radiometer," *NASA Tech. Mem. 104566* **31**, pp. 1–76, 1995.
8. U. S. Naval Observatory, *Multiyear Interactive Computer Almanac: 1990-2005*, Willmann-Bell, Richmond, VA, 1998.
9. M. E. Davies, V. K. Abalkin, M. Bursa, G. E. Hunt, J. H. Lieske, B. Morando, R. H. Rapp, P. K. Seidelmann, A. T. Sinclair, and Y. S. Tjuflin, "Report of the IAU/IAG/COSPAR working group on cartographic coordinates and rotational elements of the planets and satellites: 1989," *Celest. Mech. Dyn. Astron.* **46**, pp. 187–204, 1989.